nature nanotechnology

Article

https://doi.org/10.1038/s41565-023-01367-6

Operando characterization and regulation of metal dissolution and redeposition dynamics near battery electrode surface

Received: 14 September 2022

Accepted: 9 March 2023

Published online: 20 April 2023



Yuxin Zhang¹, Anyang Hu ¹, Dawei Xia¹, Sooyeon Hwang ² ⋈, Sami Sainio³, Dennis Nordlund³, F. Marc Michel ⁴, Robert B. Moore ^{1,5}, Luxi Li ⁶ ⋈ & Feng Lin ^{1,5,7} ⋈

Mn dissolution has been a long-standing, ubiquitous issue that negatively impacts the performance of Mn-based battery materials. Mn dissolution involves complex chemical and structural transformations at the electrode-electrolyte interface. The continuously evolving electrodeelectrolyte interface has posed great challenges for characterizing the dynamic interfacial process and quantitatively establishing the correlation with battery performance. In this study, we visualize and quantify the temporally and spatially resolved Mn dissolution/redeposition (D/R) dynamics of electrochemically operating Mn-containing cathodes. The particle-level and electrode-level analyses reveal that the D/R dynamics is associated with distinct interfacial degradation mechanisms at different states of charge. Our results statistically differentiate the contributions of surface reconstruction and Jahn-Teller distortion to the Mn dissolution at different operating voltages. Introducing sulfonated polymers (Nafion) into composite electrodes can modulate the D/R dynamics by trapping the dissolved Mn species and rapidly establishing local Mn D/R equilibrium. This work represents an inaugural effort to pinpoint the chemical and structural transformations responsible for Mn dissolution via an operando synchrotron study and develops an effective method to regulate Mn interfacial dynamics for improving battery performance.

Mn-containing battery materials can increase sustainability and reduce the cost of mass-produced rechargeable batteries¹⁻⁶. However, most of these materials can undergo degradation due to the interplay between Jahn–Teller (J–T) distortion in active Mn species and irreversible structural changes during battery operation⁷⁻¹¹. Many of the degradation processes originate at the electrochemical interface

and are interconnected at the nanometric scale¹²⁻¹⁵. Understanding the relationships between different interfacial processes (that is, particle-to-particle and particle-to-electrolyte relationship) has been a long-standing challenge for the battery community. In commercial non-aqueous Li-ion batteries, the high vapour pressure of non-aqueous solvents and air-sensitive salt prohibit the observation of interfacial

¹Department of Chemistry, Virginia Tech, Blacksburg, VA, USA. ²Center for Functional Nanomaterials, Brookhaven National Laboratory, Upton, NY, USA. ³Stanford Synchrotron Radiation Lightsource, SLAC National Accelerator Laboratory, Menlo Park, CA, USA. ⁴Department of Geosciences, Virginia Tech, Blacksburg, VA, USA. ⁵Macromolecules Innovation Institute, Virginia Tech, Blacksburg, VA, USA. ⁶Advanced Photon Source, Argonne National Laboratory, Lemont, IL, USA. ⁷Department of Materials Science and Engineering, Virginia Tech, Blacksburg, VA, USA. ⊠e-mail: soohwang@bnl.gov; luxili@anl.gov; fenglin@vt.edu

evolution under operating conditions. As such, most previous studies utilized ex situ characterizations to probe the electrode surface after cycling 9,16-18, lacking temporal resolution. Furthermore, in situ techniques such as transmission electron microscopy (TEM) show excellent temporal and spatial resolution but typically lack the statistical specificity for a complex and heterogeneous electrode surface 19,20. Thus, particle and electrode heterogeneities were rarely considered, although they play an important role in the degradation mechanism and battery performance. Therefore, a multidimensional operando investigation of Mn-based cathodes is urgently needed to statistically elucidate the dynamics of cathode surface and degradation mechanisms with temporal and spatial resolution.

Spinel LiMn $_2O_4$ (LMO) represents one of the most classical Mn-based cathodes in rechargeable Li-ion batteries $^{21-24}$. During battery cycling, the electrochemical interface deviates from equilibrium, resulting in various interfacial degradations. It is widely argued that driven by Mn $^{3+}$ J–T distortion and 2Mn $^{3+}$ \rightarrow Mn $^{2+}$ + Mn $^{4+}$ disproportionation, LMO suffers from pronounced Mn dissolution accelerated by the proton at the electrode–electrolyte interface, which aggravates the electrolyte decomposition and impedance growth on the anode surface 7,16,25 . The dissolution can also be associated with surface reconstruction 18 , that is, the formation of Mn $_3O_4$, layered or rocksalt phases, at higher voltages (>4.2 V versus Li/Li $^+$) 9,26 . However, the interplay between distinct mechanisms remains elusive and calls for a more comprehensive study.

Mn redeposition is another crucial issue that is even more insufficiently investigated. Dissolved metal cations can deposit onto the electrode surface under an electric field^{8,27}. Ion speciation across the electrochemical interface, especially metal dissolution/redeposition (D/R) dynamics, will further modify the chemistry and structure of electrode surfaces, giving rise to varied cell performances and making the surface analysis highly challenging^{8,27-31}. Tracking D/R dynamics at the electrode level can reveal the metal dissolution mechanism and quantitatively correlate the Mn loss with performance decay. Although the influences of dissolved Mn on the properties of battery components (that is, cathode, anode and electrolyte) have attracted extensive research attention^{25,27,32}, the metal D/R dynamics and mechanisms at different states of charge (SOCs) are poorly understood because reactions are spatially confined at the electrochemical interface and dynamically evolve, imposing challenges for experimental measurements.

The regulation and suppression of Mn dissolution constitutes an important factor in practical applications of Mn-based cathodes. Trapping the dissolved Mn species via coating to manipulate the Mn D/R dynamics is a promising direction but lacks exploration. Considering that the sulfonate groups in a polymer can coordinate with transition metal cations and affect the transport kinetics of different ions^{33,34}, introducing foreign polymer additives into Mn-based cathodes is a potential approach to effectively inhibit Mn dissolution.

Since LMO has decent structural integrity in neutral water at the pristine state, the LMO-based electrode operated in a dilute aqueous electrolyte offers a desirable platform for the operando observation of Mn D/R dynamics. Therefore, in this work, we report the real-time visualization and quantification of D/R dynamics with single-particle resolution and electrode-scale statistical analyses. We reveal the SOC-dependent Mn dissolution mechanisms of LMO cycled in an aqueous electrolyte. J-T distortion is the root cause for Mn dissolution at low SOCs (<1.0 V versus Ag/AgCl). When the voltage is higher than 1.0 V versus Ag/AgCl, surface reconstruction and J-T distortion coexist and impose different effects on Mn dissolution. Specifically, surface-reconstruction-induced Mn dissolution dominates the medium-voltage range (MV) (1.00–1.20 V versus Ag/AgCl), and the J-T-distortion-induced Mn dissolution governs the high-voltage range (HV) (1.20–1.55 V versus Ag/AgCl). Sulfonated tetrafluoroethylene (that is, Nafion), present at the surface of active particles, strongly coordinates with dissolved Mn cations, reduces proton conductivity,

and improves cell kinetics and cycle life. The present study creates insights into manipulating Mn D/R dynamics at the electrochemical interface for rechargeable batteries.

Dynamic Mn D/R behaviours during electrochemical cycling

We choose a 2 M lithium bis(trifluoromethanesulfonyl)imide (LiTFSI) aqueous electrolyte to investigate the Mn D/R dynamics in the LMO electrode. Such a dilute electrolyte can accelerate Mn dissolution to a quantifiable concentration within a short cycling period, allowing for in situ and operando studies. Figure 1a shows the cyclic voltammetry (CV) data of phase-pure LMO (Supplementary Fig. 1), with a pair of oxidation/reduction peaks corresponding to the Mn³⁺/Mn⁴⁺ redox couple. The high current density near the upper-cutoff voltage is collectively contributed by the Mn oxidation reaction and oxygen evolution reaction (OER). Materials degradation can be observed by the gradual peak current decay within 15 cycles. We then applied the in situ X-ray fluorescence microscopy (XFM) method35 to track Mn distribution at the electrode level throughout electrochemical cycling (Extended Data Fig. 1). The pristine drop-cast LMO electrode shows a heterogeneous Mn distribution (Fig. 1b) with some aggregated regions. Due to Mn dissolution, continuous CV cycling lowers the intensity of the high-concentration regions and reduces the overall heterogeneity of Mn distribution. We then program the data acquisition time for each XFM map to be identical to the time needed for each CV cycle, which allows us to track the net Mn concentration change following each cycle. We observe that the Mn concentration exhibits a monotonic decrease within the first ten cycles and then becomes stabilized in the following cycles (Fig. 1c). The net concentration change presented here reflects that the Mn D/R process favours dissolution until an equilibrium is reached after ten CV cycles.

We subsequently program the data acquisition time for each XFM map to be longer than the time needed for each CV cycle, which allows each XFM map to cover more than one complete CV cycle. The Mn concentration exhibits non-monotonic fluctuations (Fig. 1d), which suggests the voltage-dependent D/R behaviours. Indeed, when we perform chronoamperometry (CA) measurements at different potentials, the Mn concentration decreases at the positive potential (0.9 V) and increases at the negative potential (-0.1 V) (Supplementary Figs. 2 and 3).

We further conduct pixel-by-pixel mathematical subtractions between neighbouring maps (Supplementary Fig. 4) to obtain spatially resolved Mn concentration changes between adjacent CV cycles. The negative and positive concentration changes correspond to Mn net concentration loss (dissolution > redeposition) and net concentration gain (redeposition > dissolution) between neighbouring maps, respectively (Fig. 1e). The subtraction between the second and third cycle yields a broader and more negatively shifted histogram, indicating that Mn D/R is more heterogeneous and there is a net Mn concentration loss during the early cycles. In contrast, subtraction between the fourteenth and fifteenth cycle yields a narrower histogram centred at a 0% relative concentration change. A comparison between the two subtractions further demonstrates a more pronounced dissolution behaviour during early cycles, consistent with the data in Fig. 1c. Since LMO particles are susceptible to dissolution and redeposition once they are electrochemically cycled, we conjecture the pixels that experience a 0% relative concentration change are electrochemically inactive LMO domains. As shown in Supplementary Fig. 5, the inactive domains significantly expand after the eighth cycle. Note that the value could be overestimated owing to the possibility that a small fraction of active LMO particles may remain stable with no Mn dissolution during electrochemical cycling. In summary, the D/R dynamics decreases the redox-active Mn species and increases the population of inactive LMO domains, contributing to the performance decay. The distinct D/R dynamics during CV cycling, especially non-monotonicity, motivates us to investigate the voltage-dependent D/R dynamics.

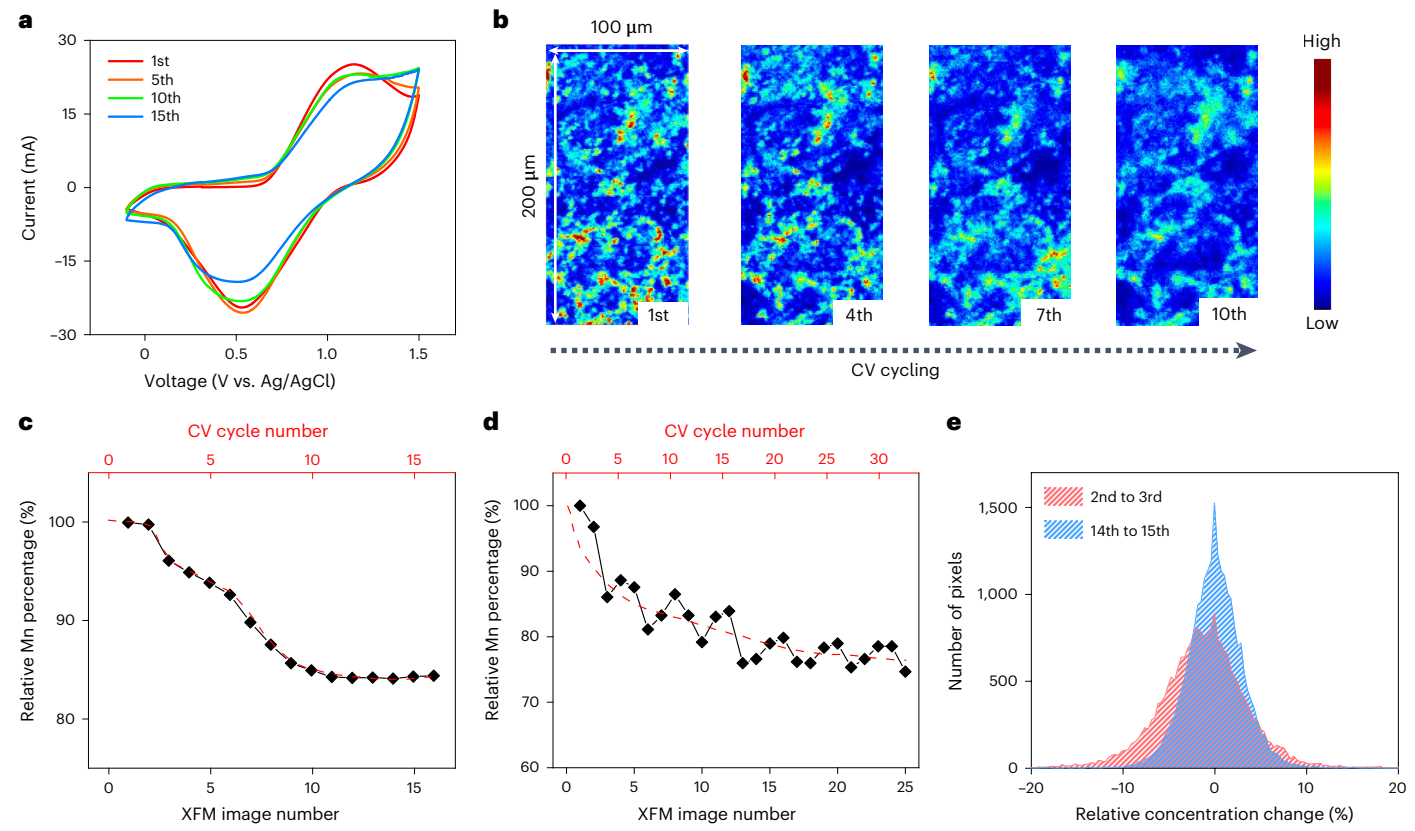


Fig. 1 | Dynamic Mn D/R process during CV cycling in the three-electrode configuration. a, CV profiles of the LMO electrode cycled in a 2 M LiTFSI aqueous electrolyte, where the scan voltage ranges from -0.1 to 1.5 V versus Ag/AgCI and the scan rate is 5 mV s $^{-1}$. b, In situ XFM mapping of the LMO electrode during CV cycling, where the colour code denotes the relative Mn concentration. The pixel size is $2~\mu m \times 2~\mu m$ and the maps are acquired from the first, fourth, seventh and tenth cycle, respectively. c, Relative Mn concentration change calculated from each XFM scan when the time required for each XFM scan (8 min 10 s) is identical to the time per CV cycle (8 min 10 s, 6.5 mV s $^{-1}$), showing continuous

Mn dissolution until stabilization after ten cycles. \mathbf{d} , Relative Mn concentration change calculated from each XFM scan when the time required for each XFM scan (14 min 10 s) is longer than the time per CV cycle (10 min 40 s, 5 mV s $^{-1}$), showing non-monotonic Mn concentration changes. \mathbf{e} , Distribution of relative Mn concentration variation at the beginning and final stages of CV cycling in \mathbf{c} through pixel-by-pixel analyses. The histogram is obtained by subtracting the corresponding pixel values between two neighbouring CV cycles, where a negative value represents Mn dissolution being more than redeposition and a positive value represents Mn redeposition being more than dissolution.

Voltage-dependent Mn D/R dynamics

LMO shows noticeable capacity decay when cycled in the 2 M LiTFSI aqueous electrolyte using the constant-current charging-discharging method (Fig. 2a). We then investigate the voltage-dependent Mn dissolution with single-particle resolution during the first charging process (Fig. 2b). The Mn concentration gradually decreases during charging, accompanied by a dramatic particle shrinkage above 1.0 V. The quantitative analysis (Fig. 2c) and corresponding first derivatives of the curve (Supplementary Fig. 6) reveal that the Mn concentration exhibits more severe loss when the voltage is higher than 1.0 V. The data point at ~1,700 s (Supplementary Fig. 6) deviates from the neighbouring points and could originate from systematic errors (that is, signal fluctuations). The apparent Mn dissolution rate is facilitated between 1.0 and 1.2 V and gets more facilitated when held at 1.2 V. More detailed analyses of different particles reveal that the Mn concentration variation ranges from -60% to +4% at the single-particle level (Extended Data Fig. 2), which could be impacted by the position of the particles in the electrode and interaction with the neighbouring particles. Therefore, an electrode-level analysis with ensemble-averaged information from many particles can represent the overall Mn D/R behaviours during cycling.

At the electrode level, we further divide the in situ first charging profile into the low-voltage range (LV) (0.30–1.00 V), MV (1.00–1.20 V) and HV (1.20 V–1.55 V) (Fig. 2d). The charging capacity at LV and MV is contributed by Mn oxidation, and the capacity at HV is attributed to

OER. From Fig. 2e, we can observe that compared with the sluggish Mn loss at the LV range, rapid Mn dissolution takes place at the MV and beginning of HV ranges. Moreover, during the holding process at 1.2 V, we can notice that the Mn concentration experiences a severe drop at the initial stage (Fig. 2e), in line with the feature we observed at the single-particle level (Fig. 2c) and corresponding to a high dissolution rate, and it gets stabilized on elongated voltage holding at 1.2 V, suggesting a dynamic equilibrium of dissolution and redeposition processes. The accumulated Mn loss is 3.0%, 3.8% and 3.5% at LV, MV and HV, respectively, which shows that medium-voltage charging, although providing only 21 mA g⁻¹ capacity (23% of the total charge capacity), introduces the most severe Mn dissolution. The Mn D/R behaviours in the following charging processes exhibit a non-monotonic feature and become more complicated (Supplementary Fig. 7), which could be attributed to the further interaction between electrode particles and gradually accumulated Mn species at the electrode-electrolyte interface. The overall Mn loss shows large discrepancy between the single-particle and electrode-scale measurements. Between OCV and 1.2 V, the single-particle measurement has a 40.4% loss, whereas the electrode-scale measurement has a 6.8% loss. Some particles experience higher degrees of redox reactions and therefore a more severe Mn dissolution behaviour than other particles, indicating a heterogeneous charge distribution at the electrode level^{36,37}. Moreover, at both MV and HV ranges, we observe a Gaussian-like distribution in the pixel-by-pixel

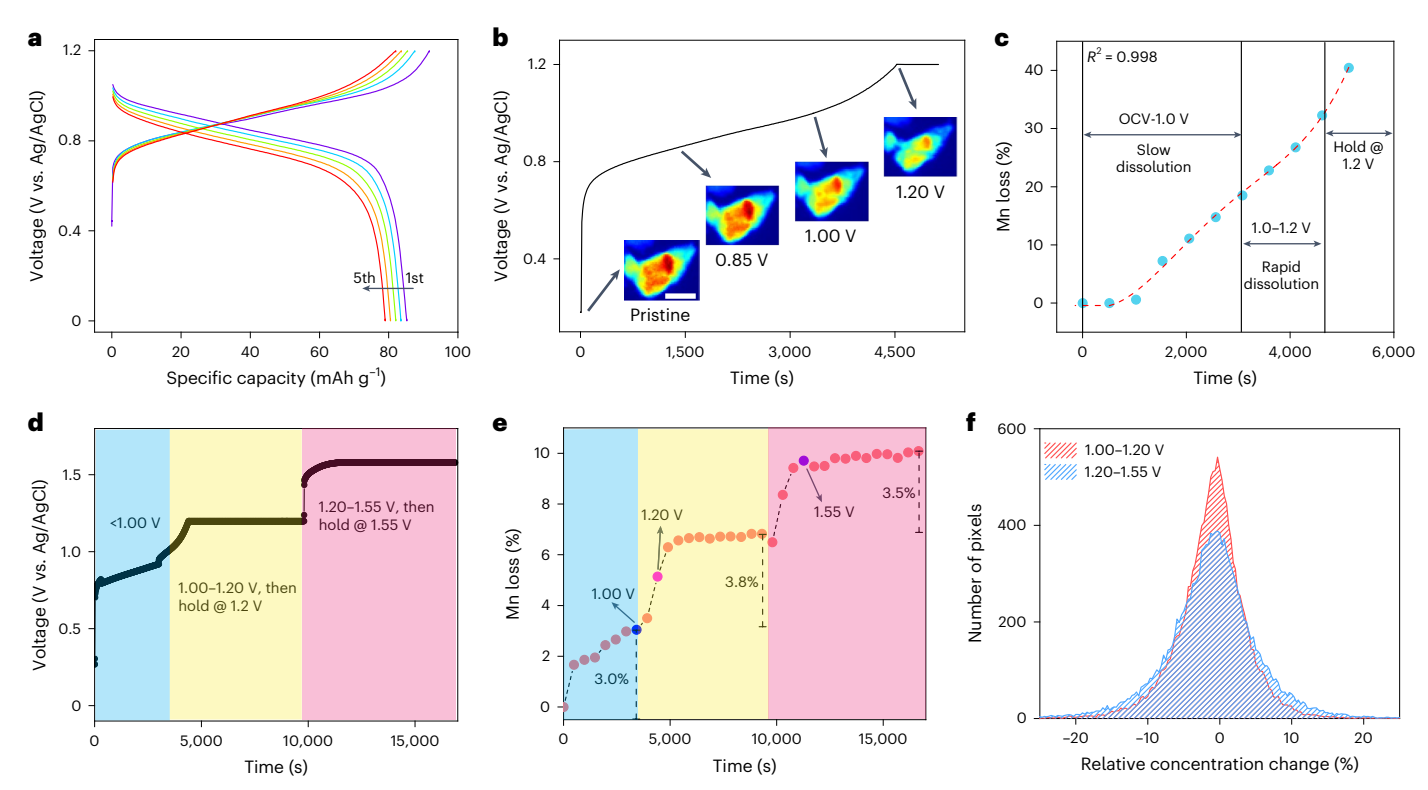


Fig. 2 | **Voltage-dependent Mn dissolution behaviours. a**, Charge–discharge profiles of the LMO electrode in the 2 M LiTFSI aqueous electrolyte, where the voltage range is 0–1.2 V versus Ag/AgCI and the current density is 1 C (100 mA g^{-1}). **b**, The first charging profile (-0.8 C) of in situ XFM measurements and the corresponding particle-level Mn concentration maps at different charging voltages. The pixel size is 300 nm \times 300 nm and the image size is 12 μ m \times 15 μ m. **c**, Particle-level Mn loss ratio calculated from the results in **b**. **d**, The first charging

profile (-0.8 C) of in situ XFM measurements for electrode-level analyses, where the voltage was kept constant at 1.20 and 1.55 V for additional XFM measurements. The blue, yellow and pink background colours represent LV, MV and HV, ranges, respectively. \mathbf{e} , Electrode-level Mn loss ratio during charging. The voltage-holding processes start from the data points labelled with 1.20 and 1.55 V. \mathbf{f} , Pixel-by-pixel analyses of Mn D/R dynamics at the MV and HV ranges.

analyses of the Mn D/R dynamics (Fig. 2f), which suggests that both Mn dissolution and redeposition take place when the LMO undergoes charging. Meanwhile, by using graphite paper as the counter electrode, we show that the dissolved species can not only redeposit on the LMO surface but also migrate through the electrolyte and deposit on the counter electrode (Extended Data Fig. 3). Overall, our results show a voltage-dependent, continuously evolving Mn D/R behaviour on constant-current charging.

Voltage-dependent structural and chemical transformations

To shed light on the Mn dissolution mechanism at different voltage ranges, we apply in situ hard X-ray absorption spectroscopy (XAS) to investigate the bulk properties of LMO on cycling. We select five SOCs, namely, pristine, 1.00 V, 1.20 V, 1.45 V and discharged states (Fig. 3a). Based on the white-line energy of the reference and LMO samples, we show that Mn is continuously oxidized from 3.5+ at the pristine state to 3.9+ at the 1.2 V charged state, whereas it demonstrates negligible change at the HV region (Fig. 3b-d). Extended X-ray absorption fine structure (EXAFS) (Fig. 3e) reveals that Mn-O and Mn-Mn interatomic distances experience abnormal elongation when LMO enters the HV range (Fig. 3f). The EXAFS fitting results show that the corresponding Mn-O coordination number is reduced from six to five (Fig. 3g, Supplementary Figs. 8 and 9 and Supplementary Tables 1–5). These results collectively reveal the structural degradation of LMO induced by the OER at HV, originating from the lattice oxygen loss³². Since the particle surface can directly interact with the electrolyte, it is expected that the surface will undergo the most pronounced structural change on cycling, as confirmed by previous studies regarding the surface reconstruction in layered cathode materials 18 . Therefore, understanding the surface structural change is crucial to reveal the LMO degradation mechanism in aqueous electrolytes.

To gain more insights into the surface reconstruction of LMO on charging, we conduct a suite of surface-sensitive characterizations. The high-angle annular dark-field scanning transmission electron microscopy (HAADF-STEM) images along the [110] zone axis of pristine materials confirm a well-defined spinel LMO phase from particle surface to bulk (Supplementary Fig. 10). After charging to 1 V, a transition phase between spinel LMO and Mn_3O_4 appears on the surface (Supplementary Fig. 11)⁹, which is further transformed to pure Mn₃O₄ phase when the electrode is charged to 1.2 V (Supplementary Fig. 12). Meanwhile, the intensity of Mn atoms with a lower stacking density gets greatly diminished at the surface, and such a feature becomes more pronounced in the 1.55 V charged particles (Supplementary Fig. 13). The Mn dissolution behaviour of Mn₃O₄ (Extended Data Fig. 4) and MnO₂ (Extended Data Fig. 5) proves that Mn loss at 1.2 V mainly originates from Mn₃O₄ dissolution owing to the relatively weak chemical bond between Mn²⁺ and oxygen anions. The Mn L_{2,3} electron energy loss spectra (EELS) of the 1.55 V charged LMO particles exhibit blueshift (Fig. 3h,i) moving from the surface to the bulk, confirming that Mn is reduced on the surface. The thickness of the surface reduction layer is estimated to be ~10 nm, consistent with the thickness of the distorted region in the HAADF-STEM image (Supplementary Fig. 13). We believe that such a thick surface reconstruction layer is caused by the thermodynamic instability of the delithiated LMO and the electrode-electrolyte side reaction. After 20 cycles, the particle becomes porous with polycrystalline structures and amorphous phases emerging on the surface (Supplementary Fig. 14), suggesting a severe distortion of the LMO

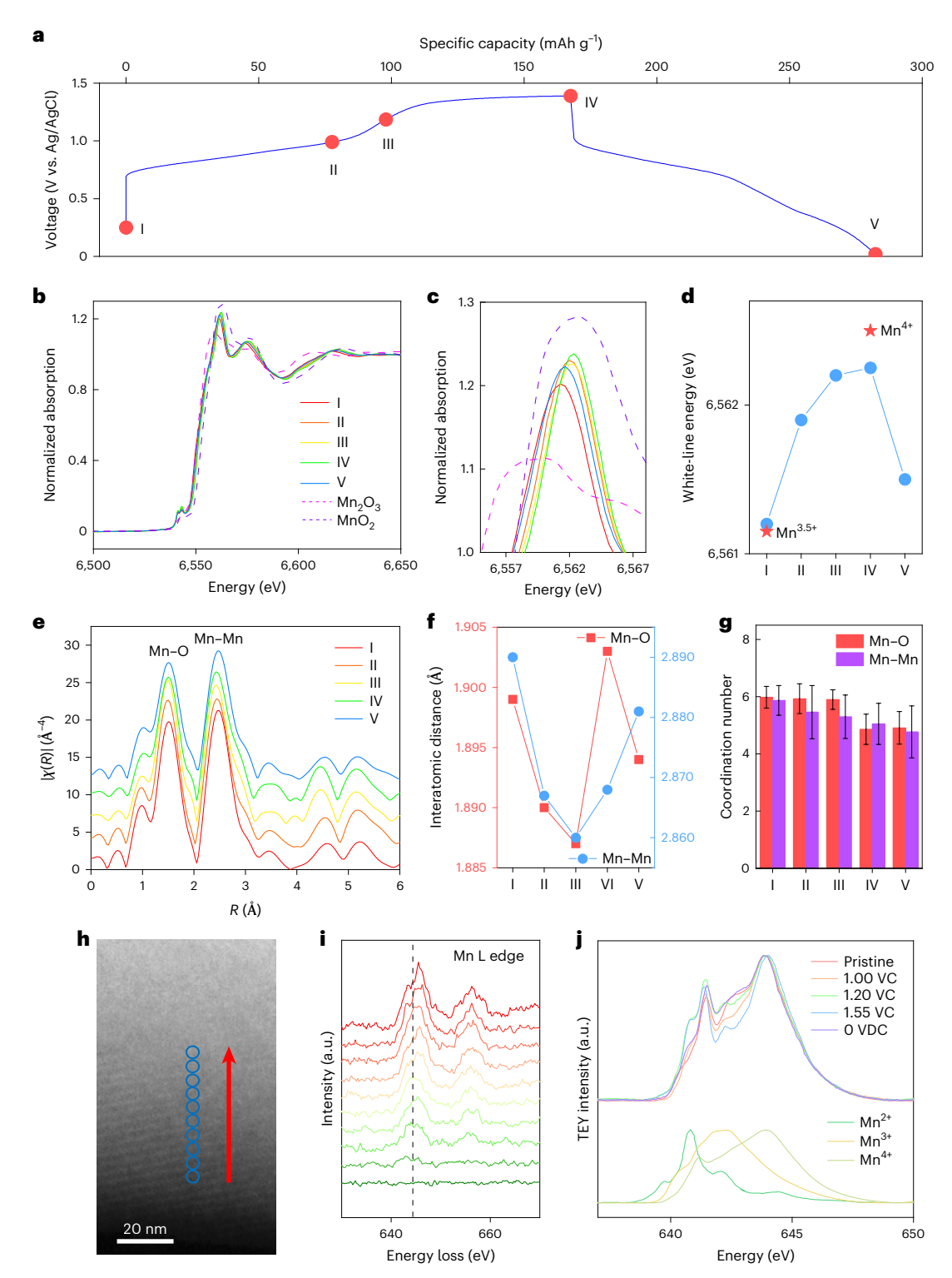
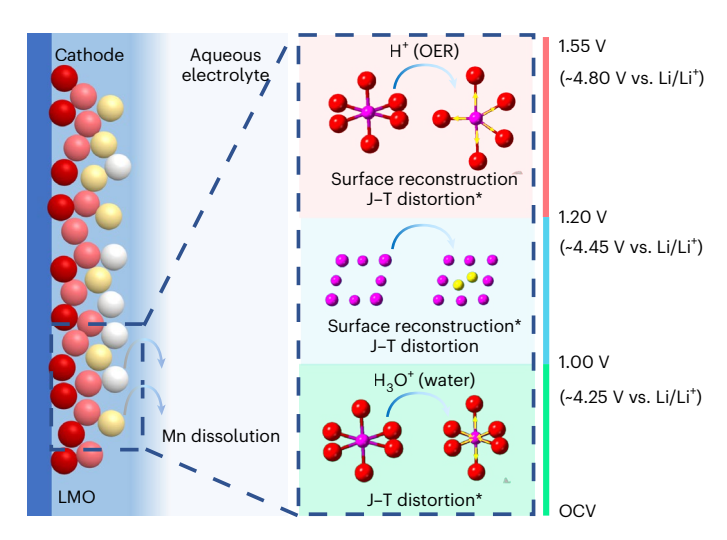


Fig. 3 | Chemical and structural transformations of LMO during electrochemical cycling. a, Charge–discharge profile of in situ hard XAS measurements, where the current density is $0.2 \, \mathrm{C} \, (20 \, \mathrm{mA \, g^{-1}})$. b, c, Mn K-edge hard XAS spectra at different SOCs (b) and the corresponding zoomed-in views of the white-line region (c). d, White-line energy as a function of SOCs. e, Fourier-transformed magnitude of Mn K-edge EXAFS at different SOCs. f, Interatomic distance at different SOCs. g, Coordination numbers for Mn–O and Mn–Mn

obtained from Mn K-edge EXAFS simulations. The error bars are generated on the basis of the EXAFS simulation errors. \mathbf{h} , HAADF-STEM image for the scanning pathway. \mathbf{i} , Mn L $_{2.3}$ -edge EELS spectra along the scanning pathway. \mathbf{j} , Mn L $_{3}$ -edge soft XAS spectra of LMO electrodes at different SOCs. For example, 1.55 VC indicates the electrode charged to 1.55 V, and 0 VDC indicates the electrode discharged to 0 V. The measurements were conducted using the surface-sensitive TEY mode .

structure in dilute aqueous electrolytes. The soft XAS results show that LMO undergoes a typical oxidation process on charging to $1\,V$ (Fig. 3j). However, on charging to $1.20\,V$ (MV) and $1.55\,V$ (HV), Mn at the surface

becomes reduced, in agreement with the EELS results and confirming the emergence of surface reconstruction. The appearance of the mixed states of Mn^{2+} and Mn^{3+} species at MV proves the formation of Mn_3O_4



 $\label{lem:prop:section} \textbf{Fig. 4} \ | \ \textbf{Mn} \ dissolution \ mechanism \ of \ LMO \ in \ 2 \ M \ LiTFSI \ aqueous \ electrolytes. \\ Schematic of the voltage-dependent Mn \ dissolution mechanisms, where the asterisk symbol indicates the primary degradation-driving forces. The different colours of LMO particles indicate different SOCs, where the red colour suggests the highest SOC, whereas the white colour suggests the lowest SOC. The particles close to the current collector exhibit higher SOC compared with the particles far from the current collector. The yellow arrow indicates the change in bond length. The OCV stands for open-circuit voltage.$

on the particle surface, which agrees with previous observations in non-aqueous electrolytes 9 . These findings suggest that a higher degree of structural distortion occurs when the voltage is higher than 1 V. On discharging to 0 V, the surface becomes more oxidized than that at 1.20 V (MV) and 1.55 V (HV), which suggests that Mn $_3$ O $_4$ gets dissolved on discharging, consistent with the hard XAS results (Fig. 3). Collectively, our results show that there is correlation between surface reconstruction and Mn dissolution.

Correlations between Mn D/R dynamics and LMO transformations

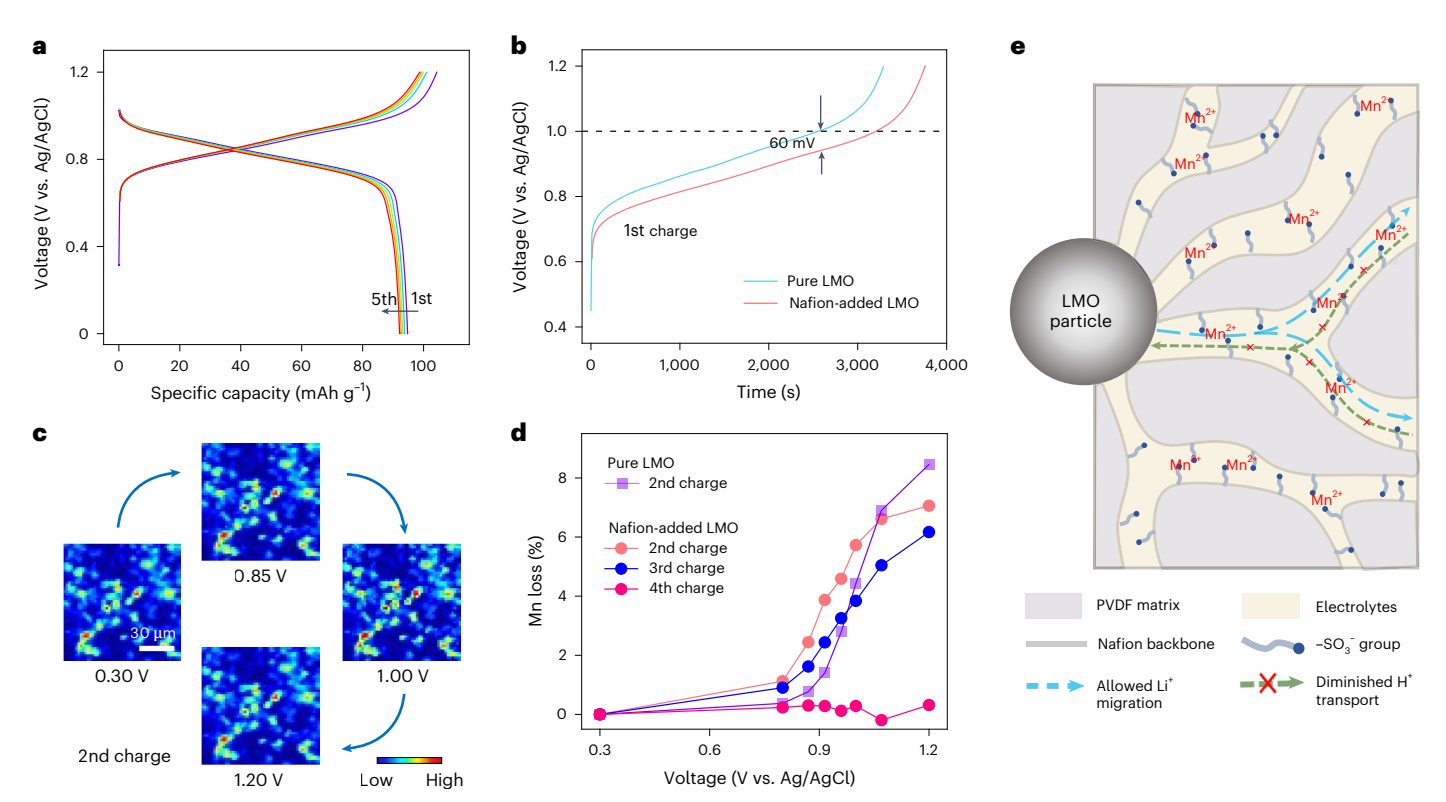
Thus far, our study has found that both D/R dynamics and materials transformation are voltage dependent. Since Mn dissolution has been shown to be strongly correlated with materials transformation ^{7,16}, here we statistically establish the correlation between D/R dynamics and materials transformation at different voltage ranges.

Mn concentration in a pristine electrode exhibits non-uniform distribution in the histogram (Supplementary Fig. 15a), suggesting the heterogeneous loading of the as-prepared LMO electrode. We divide the initial electrode loading into four categories based on the Mn XFM concentration map, namely, low C, medium-low C, medium-high C and high C. The area under the curve in the concentration histogram reflects the total Mn concentration and is used to separate different categories, where each category occupies 25% of the area under the curve (Supplementary Fig. 15a). Meanwhile, at each voltage range, we can categorize the D/R dynamics into four scenarios based on the net change of the local Mn concentration, that is, mild net dissolution, mild net redeposition, severe net dissolution and severe net redeposition (Supplementary Fig. 15b). These two categorizations allow us to quantitatively correlate the D/R dynamics, initial LMO loading and voltage range. By comparing the D/R dynamics with the same scenario (that is, same colour-coded data points; Supplementary Fig. 16) at different voltage ranges, we observe that the LV and HV ranges display similar characteristics and are distinct from the MV range (Supplementary Fig. 16). Therefore, the driving force behind the D/R dynamics at the LV and HV ranges is distinct from that at the MV range.

Combined with the characterization results (Fig. 3), we propose the correlation between D/R dynamics and voltage-dependent materials transformations (Fig. 4). When LMO is charged from 0.3 V to 1.0 V (LV range), a substantial amount of Mn still remains at the J-Tactive Mn³⁺ state due to the low charge capacity (low Mn oxidation), leading to noticeable Mn dissolution in the presence of hydronium in the water. When the voltage is between 1.0 and 1.2 V, the delithiated LMO particles undergo surface reconstruction and the emergence of soluble Mn²⁺ in Mn₃O₄ dominates the Mn dissolution behaviour. Once the LMO is further charged to the OER potential (that is, HV range), protons gradually accumulate near the electrode surface due to the decreased OH⁻ concentration caused by the OER. Since the capacity of LMO is smaller than the theoretical value (148 mAh g⁻¹) and our hard XAS results (Fig. 3g) show that Mn is not fully oxidized at 1.55 V, many particles remain partially charged even at the HV range, indicating heterogeneous charge distribution at the electrode level (particle with different colour codes; Fig. 4), which is associated with the different Mn D/R behaviours at the particle level (Extended Data Fig. 2). The enriched proton species near the electrode surface aggravates the disproportion of residual Mn3+ and makes the J-T-distortion-induced Mn dissolution become the primary factor responsible for Mn dissolution. Moreover, the acidic environment drastically interferes with the Mn local bonding and induces more lattice oxygen loss compared with the LV range (Fig. 3g). Therefore, the dissolution rate at the HV range is significantly boosted (Fig. 2e). We believe that the Mn D/R dynamics and corresponding degradation mechanisms presented here can also provide insights into a non-aqueous system, where the proton species are generated by the ethylene carbonate and LiPF₆ interacting with trace moisture in the electrolytes. In other words, Mn dissolution should be inhibited in the electrolytes with negligible proton species. Therefore, we also evaluate the Mn D/R behaviour of LMO in organic solvents. Here tetraethylene glycol dimethyl ether with a low vapour pressure is selected as the solvent. As shown in Extended Data Fig. 6, Mn dissolution is significantly inhibited in 2 M LiTFSI-tetraethylene glycol dimethyl ether electrolytes owing to the reduced proton concentration. The accumulative Mn loss is estimated to be ~1.5% on the first charging process, and the protons generated as a result of ether decomposition is the primary reason that leads to Mn dissolution³⁸. It should be noted that the sealing of our operando cell is less stringent than that of a coin-cell or pouch-cell configuration, and the net Mn dissolution could be overestimated in this case due to moisture impact.

Regulating Mn D/R dynamics with sulfonated polymers

Our results have revealed that surface reconstruction at the MV range leads to the most severe Mn dissolution when the upper-cutoff voltage is set to 1.2 V versus Ag/AgCl. Hence, inhibiting surface reconstruction is expected to improve the performance. Nafion, a cation-exchange polymer that allows for the selective permeation of cations, has been widely utilized as a coating material in fuel cells and catalysts to reduce undesired interfacial interactions and alleviate surface degradation^{33,34,39,40}. Here we discover that simply adding Nafion during electrode preparation can efficiently mitigate the capacity loss of the composite electrode during cycling. As shown in Fig. 5a, the capacity retention of Nafion-added LMO is improved. Compared with pure LMO, the Nafion-added LMO electrode exhibits smaller reaction overpotentials at the LV range and a higher output capacity (Fig. 5b). The TEM results (Supplementary Fig. 17) reveal that the Mn₃O₄ phase appears on the particle surface after Nafion coating owing to the acidic environment in the Nafion solution. The Mn²⁺ species in Mn₃O₄ can be easily dissolved into the electrolyte at low voltages, thereby giving rise to more Mn loss at the LV range during in situ XFM measurements. (Fig. 5c,d). In contrast, at the MV range (1.0–1.2 V), the Nafion layer can modify the interaction between LMO and aqueous electrolytes and suppress Mn dissolution. Importantly, the Nafion-added LMO electrode



 $\label{lem:continuous} \textbf{Fig. 5} | \textbf{Electrochemical performance and underlying Mn dissolution} \\ \textbf{behaviour of Nafion-added LMO materials. a,} & \textbf{Charge-discharge profiles of Nafion-added LMO electrodes in the 2 M LiTFSI aqueous electrolyte, where the voltage range is 0-1.2 V versus Ag/AgCl and the current density is 1 C (100 mA g^-1).} \\ \textbf{b,} & \textbf{Comparison of the first charging curve of pure LMO and Nafion-added LMO,} \\ \textbf{where the Nafion-added LMO shows smaller overpotentials on charging. c, In situ$

XFM mapping of the Nafion-added LMO at different SOCs, where the colour code denotes the Mn concentration. The pixel size is $2\,\mu\text{m}\times2\,\mu\text{m}$ and the image size is $100\,\mu\text{m}\times100\,\mu\text{m}$. **d**, Mn loss of pure LMO and Nafion-added LMO electrodes on charging. **e**, Schematic of the chemical environment surrounding Nafion-added LMO particles during the fourth charging process.

exhibits negligible net Mn loss at the fourth charge. As shown in Fig. 5e, this phenomenon could be attributed to the fact that the sulfonate groups in Nafion can ionically associate with the positively charged Mn species and reduce the proton-hopping sites⁴¹, which effectively diminishes the proton transport and prevents the surface from the attack of protons. Meanwhile, trapped Mn²⁺ can accumulate near the particle surface, reducing the time needed to reach D/R equilibrium (that is, Le Chatelier's principle). These two factors collectively lead to suppressed Mn loss in the following cycles. To further validate our hypothesis, we soak the cast Nafion membrane into a 2 M MnSO₄ aqueous solution for 1 day. The energy-dispersive X-ray spectroscopy results confirm the significantly increased Mn concentration in the soaked membranes, and the atomic ratio of S:Mn can reach 1.85, suggesting over 50% sulfate groups coordinate with the Mn species (Extended Data Fig. 7). Therefore, introducing Nafion into the composite electrodes can improve the reaction kinetics, regulate Mn dissolution and significantly mitigate Mn loss. We also want to highlight that controlling the Nafion concentration is crucial in maintaining the LMO structure and improving the performance. Excessive Nafion solution can lead to rapid capacity decay due to the instability of the LMO phase in acidic environments (Supplementary Fig. 18). In our study, the weight ratio of LMO:Nafion is controlled to be larger than 150. Moreover, using deprotonated Nafion is another strategy to alleviate LMO structural changes during the modification process.

Conclusion

Understanding and controlling the dynamic Mn D/R behaviours in Mn-based cathodes can reveal the electrode degradation mechanisms and more importantly inform the development of methods for

stabilizing electrode materials. The continuously evolved speciation at the electrochemical interface makes it challenging to accurately identify the interfacial degradation processes, such as metal dissolution. Using in situ XFM and a suite of surface- and bulk-sensitive techniques, we have developed a comprehensive understanding about the Mn D/R dynamics and the corresponding LMO degradation mechanism in an aqueous electrolyte. Continuous Mn dissolution and increased inactive LMO domains collectively lead to performance decay on cycling. J-T distortion and surface reconstruction are responsible for the voltage-dependent Mn dissolution behaviour. Mn dissolution exhibits a nonlinear relationship with voltage, and a higher rate can be observed when surface reconstruction takes place. Introducing Nafion into the electrodes can boost the reaction kinetics and inhibit Mn dissolution, especially that caused by surface reconstruction. Meanwhile, trapped Mn²⁺ in Nafion can hinder proton diffusion towards the LMO particle surface and accelerate the establishment of Mn D/R equilibrium, thereby improving the cycle life in a dilute electrolyte. The present study directly visualizes and quantifies transition metal D/R dynamics and unravels the role of a sulfonated polymer in controlling the D/R dynamics and improving the battery performance. The in situ experimental methods developed here can be broadly applied to investigate other electrochemical systems that involve solid-liquid interfaces.

Online content

Any methods, additional references, Nature Portfolio reporting summaries, source data, extended data, supplementary information, acknowledgements, peer review information; details of author contributions and competing interests; and statements of data and code availability are available at https://doi.org/10.1038/s41565-023-01367-6.

References

- Thackeray, M. M. & Amine, K. LiMn₂O₄ spinel and substituted cathodes. Nat. Energy 6, 566 (2021).
- Kim, D. K. et al. Spinel LiMn₂O₄ nanorods as lithium ion battery cathodes. Nano Lett. 8, 3948–3952 (2008).
- Xia, H., Luo, Z. & Xie, J. Nanostructured LiMn₂O₄ and their composites as high-performance cathodes for lithium-ion batteries. *Prog. Nat. Sci.: Mater. Int.* 22, 572–584 (2012).
- Lun, Z. et al. Design principles for high-capacity Mn-based cation-disordered rocksalt cathodes. Chem 6, 153–168 (2020).
- 5. Li, H. et al. Toward high-energy Mn-based disordered-rocksalt Li-ion cathodes. *Joule* **6**, 53–91 (2022).
- Zhang, Y. et al. Investigating particle size-dependent redox kinetics and charge distribution in disordered rocksalt cathodes. Adv. Funct. Mater. 32, 2110502 (2022).
- Sun, X., Xiao, R., Yu, X. & Li, H. First-principles simulations for the surface evolution and Mn dissolution in the fully delithiated spinel LiMn₂O₄. Langmuir 37, 5252–5259 (2021).
- 8. Zhan, C., Wu, T., Lu, J. & Amine, K. Dissolution, migration, and deposition of transition metal ions in Li-ion batteries exemplified by Mn-based cathodes—a critical review. *Energy Environ. Sci.* 11, 243–257 (2018).
- Tang, D. et al. Surface structure evolution of LiMn₂O₄ cathode material upon charge/discharge. Chem. Mater. 26, 3535–3543 (2014).
- Zhou, G. et al. Mn ion dissolution mechanism for lithium-ion battery with LiMn₂O₄ cathode: in situ ultraviolet-visible spectroscopy and ab initio molecular dynamics simulations. J. Phys. Chem. Lett. 11, 3051–3057 (2020).
- Zhu, X. et al. LiMnO₂ cathode stabilized by interfacial orbital ordering for sustainable lithium-ion batteries. *Nat. Sustain.* 4, 392–401 (2021).
- Lin, R. et al. Characterization of the structure and chemistry of the solid-electrolyte interface by cryo-EM leads to high-performance solid-state Li-metal batteries. Nat. Nanotechnol. 17, 768-776 (2022).
- Cao, L. et al. Fluorinated interphase enables reversible aqueous zinc battery chemistries. Nat. Nanotechnol. 16, 902–910 (2021).
- 14. Liu, T. et al. In situ quantification of interphasial chemistry in Li-ion battery. *Nat. Nanotechnol.* **14**, 50–56 (2019).
- Xiang, Y. et al. Quantitatively analyzing the failure processes of rechargeable Li metal batteries. Sci. Adv. 7. eabi3423 (2021).
- Liu, T. et al. Correlation between manganese dissolution and dynamic phase stability in spinel-based lithium-ion battery. Nat. Commun. 10, 4721 (2019).
- Xu, C. et al. Bulk fatigue induced by surface reconstruction in layered Ni-rich cathodes for Li-ion batteries. *Nat. Mater.* 20, 84–92 (2021).
- Lin, F. et al. Surface reconstruction and chemical evolution of stoichiometric layered cathode materials for lithium-ion batteries. Nat. Commun. 5, 3529 (2014).
- Liu, X. et al. Distinct charge dynamics in battery electrodes revealed by in situ and operando soft X-ray spectroscopy. Nat. Commun. 4, 2568 (2013).
- Yuan, Y., Amine, K., Lu, J. & Shahbazian-Yassar, R. Understanding materials challenges for rechargeable ion batteries with in situ transmission electron microscopy. Nat. Commun. 8, 15806 (2017).
- Jaumaux, P. et al. Localized water-in-salt electrolyte for aqueous lithium-ion batteries. Angew. Chem. Int. Ed. 60, 19965–19973 (2021).
- Suo, L. et al. 'Water-in-salt' electrolyte enables high-voltage aqueous lithium-ion chemistries. Science 350, 938–943 (2015).
- 23. Xu, J. et al. Aqueous electrolyte design for super-stable 2.5 V $\text{LiMn}_2\text{O}_4||\text{Li}_4\text{Ti}_5\text{O}_{12}|$ pouch cells. *Nat. Energy* **7**, 186–193 (2022).
- Xie, J., Liang, Z. & Lu, Y.-C. Molecular crowding electrolytes for high-voltage aqueous batteries. *Nat. Mater.* 19, 1006–1011 (2020).

- Wang, C. et al. Overlooked electrolyte destabilization by manganese (II) in lithium-ion batteries. Nat. Commun. 10, 3423 (2019).
- Leifer, N. et al. Studies of spinel-to-layered structural transformations in LiMn₂O₄ electrodes charged to high voltages. J. Phys. Chem. C 121, 9120–9130 (2017).
- 27. Vissers, D. R. et al. Role of manganese deposition on graphite in the capacity fading of lithium ion batteries. *ACS Appl. Mater. Interfaces* **8**, 14244–14251 (2016).
- Ren, Q., Yuan, Y. & Wang, S. Interfacial strategies for suppression of Mn dissolution in rechargeable battery cathode materials. ACS Appl. Mater. Interfaces 14, 23022–23032 (2021).
- Xu, W. et al. Understanding the effect of Al doping on the electrochemical performance improvement of the LiMn₂O₄ cathode material. ACS Appl. Mater. Interfaces 13, 45446–45454 (2021).
- Lee, S., Cho, Y., Song, H., Lee, K. T. & Cho, J. Carbon-coated single-crystal LiMn₂O₄ nanoparticle clusters as cathode material for high-energy and high-power lithium-ion batteries. *Angew. Chem. Int. Ed.* 51, 8748–8752 (2012).
- 31. Wandt, J. et al. Transition metal dissolution and deposition in Li-ion batteries investigated by operando X-ray absorption spectroscopy. *J. Mater. Chem. A* **4**, 18300–18305 (2016).
- 32. Gao, X. et al. Oxygen loss and surface degradation during electrochemical cycling of lithium-ion battery cathode material LiMn₂O₄. *J. Mater. Chem. A* **7**, 8845–8854 (2019).
- Santo, K. P. & Neimark, A. V. Effects of metal-polymer complexation on structure and transport properties of metal-substituted polyelectrolyte membranes. *J. Colloid Interface* Sci. 602, 654–668 (2021).
- 34. Kumar, R., Pasupathi, S., Pollet, B. G. & Scott, K. Nafion-stabilised platinum nanoparticles supported on titanium nitride: an efficient and durable electrocatalyst for phosphoric acid based polymer electrolyte fuel cells. *Electrochim. Acta* **109**, 365–369 (2013).
- 35. Kuai, C. et al. Phase segregation reversibility in mixed-metal hydroxide water oxidation catalysts. *Nat. Catal.* **3**, 743–753 (2020).
- 36. Yang, Y. et al. Quantification of heterogeneous degradation in Liion batteries. *Adv. Energy Mater.* **9**, 1900674 (2019).
- Li, J. et al. Dynamics of particle network in composite battery cathodes. Science 376, 517–521 (2022).
- Jang, D. H. & Oh, S. M. Electrolyte effects on spinel dissolution and cathodic capacity losses in 4 V Li/Li_xMn₂O₄ rechargeable cells. J. Electrochem. Soc. **144**, 3342 (1997).
- 39. Sarapuu, A., Hussain, S., Kasikov, A., Pollet, B. G. & Tammeveski, K. Electroreduction of oxygen on Nafion®-coated thin platinum films in acid media. *J. Electroanal. Chem.* **848**, 113292 (2019).
- Yang, C. et al. A novel approach to fabricate membrane electrode assembly by directly coating the Nafion ionomer on catalyst layers for proton-exchange membrane fuel cells. ACS Sustain. Chem. Eng. 8, 9803–9812 (2020).
- Sharma, P. P. & Kim, D. A facile and sustainable enhancement of anti-oxidation stability of Nafion membrane. *Membranes* 12, 521 (2022).

Publisher's note Springer Nature remains neutral with regard to jurisdictional claims in published maps and institutional affiliations.

Springer Nature or its licensor (e.g. a society or other partner) holds exclusive rights to this article under a publishing agreement with the author(s) or other rightsholder(s); author self-archiving of the accepted manuscript version of this article is solely governed by the terms of such publishing agreement and applicable law.

© The Author(s), under exclusive licence to Springer Nature Limited 2023

Methods

Materials preparation

The active material (LMO) was provided by the US Department of Energy's (DOE) Cell Analysis, Modeling and Prototyping facility at Argonne National Laboratory. LiTFSI salts (99.95%), Nafion solution (5 wt%, containing 45.00% water) and Mn $_3$ O $_4$ (97.00%) were purchased from Sigma-Aldrich. MnO $_2$ (activated; tech., 90%) was purchased from Alfa Aesar. MnO $_2$ was heated at 350 °C for 12 h in air before use.

Electrochemical measurements

In the three-electrode system, Ag/AgCl (3 M NaCl) (MF-2052, BASi Research Products) and Pt wire (Sigma-Aldrich) were utilized as the reference and counter electrodes, respectively. The electrolyte was prepared by dissolving 2 MLiTFSI in deionized water. The LMO slurry was prepared by mixing active materials, carbon black and polyvinylidene fluoride at a ratio of 8:1:1 and then drop-cast onto carbon paper. The active mass loading was estimated to be ~3 mg cm⁻². The composition (% weight) of LMO electrodes used for the particle-level analysis is 6:3:1 (LMO:polyvinylidene fluoride:carbon black) to stabilize the particle during XFM experiments. The mass loading is ~2 mg cm⁻². For the Nafion-added LMO electrodes, 45 µl Nafion solution was added to the LMO slurry containing 300 mg of solid mixture. Then, the slurry was drop-cast onto carbon paper with a mass loading of ~3.5 mg cm⁻². The composition (% weight) of drop-cast Mn₃O₄ and MnO₂ electrodes was 8:1:1 (active material:polyvinylidene fluoride:carbon black), and the mass loading was ~4 mg cm⁻². The CV measurement was conducted at a scan rate of 5 mV s⁻¹ within -0.1 to 1.5 V (versus Ag/AgCl). Galvanostatic cycling with potential limitation (normal charging-discharging process) measurement was conducted within 0-1.2 V (versus Ag/AgCl) and the current density was 100 mA g⁻¹. The CA measurements were conducted at different voltages (-0.1, 0.9, 1.2 V) for the measurements. All the electrochemical measurements were conducted using a potentiostat (SP-150, BioLogic).

Scanning electron microscopy and X-ray diffraction characterizations

The morphology of the materials was characterized using a LEO 1550 field-emission scanning electron microscope at an accelerating voltage of 6 kV. The energy-dispersive X-ray spectroscopy measurements were carried out with a scanning electron microscope at an accelerating voltage of 20 kV. The energy-dispersive X-ray spectroscopy sample of a soaked Nafion membrane is washed with deionized water three times and dried at 80 °C to remove the residual water. The lab X-ray diffraction results were obtained on a Rigaku Miniflex II diffractometer with a Cu K α X-ray radiation (λ = 1.54 Å) in a scan range of 10°-70°.

In situ XFM measurements

The in situ XFM measurements were performed at the 2-ID-E beamline of the Advanced Photon Source, Argonne National Laboratory. The in situ cell design can be found in a previous report 35 . The samples were prepared by the same drop-casting method as described above. The Ag/AgCl and carbon rod serve as the reference and counter electrodes, respectively, during the electrochemical measurements. The bulk electrodes were raster scanned by a submicrometre (-700 nm) focused 10.5 keV X-ray beam with a step size of 2 μ m for electrode-scale measurements and 300 nm for particle-level measurements along the x and y axes, except for the step size of XFM measurement (Fig. 5c), which is 2 μ m along the x and y axes. During the measurement, the samples were aligned at an angle of -60° with respect to the incident beam. The fluorescent X-ray signals were detected with a four-element silicon-drift Vortex detector, and the raw data were processed and quantified with XRF-Maps (Version: 1.8.0.00) software developed by Argonne National Lab.

In situ hard XAS measurements

Hard XAS measurements were conducted at beamline 4-1 at the Stanford Synchrotron Radiation Lightsource, SLAC National Accelerator

Laboratory. The sample preparation and cell configuration were the same as in the XFM measurements. The Mn K-edge spectra were collected in the fluorescence mode, with the samples aligned at an angle of -45° with respect to the incident beam and fluorescence detector. The Mn metal foil was used to calibrate the edge energy. All the X-ray absorption near-edge structure and EXAFS spectra were analysed with the Athena software (Version: 0.9.26). The fitting of the EXAFS results was analysed with Artemis software (Version: 0.9.26). The current density was 20 mA $\rm g^{-1}$ for the charging–discharging process during in situ XAS measurements.

TEM measurements

The HAADF-STEM and EELS measurements were performed with Thermo Fisher Talos F200X and Hitachi HD2700C instruments at an accelerating voltage of 200 kV at the Center for Functional Nanomaterials, Brookhaven National Laboratory. The background subtraction of EELS spectra was processed with DigitalMicrograph (Gatan) software (Version: 3.50.3584.0).

Soft XAS measurements

Soft XAS measurements were performed at the Stanford Synchrotron Radiation Lightsource, beamline 10-1, SLAC National Accelerator Laboratory, using a ring current of 350 mA and 1,000 lines mm $^{-1}$ spherical grating monochromator with 20 μm entrance and exit slits, providing $^{-1}0^{11}$ photons s^{-1} at 0.2 eV resolution in a 1 mm 2 beam spot. Data were acquired under an ultrahigh vacuum (10 $^{-9}$ torr) in a single load at room temperature using the total electron yield (TEY) mode, where the sample drain current was collected. The samples were mounted on an aluminium sample holder in an argon-filled glovebox and well sealed for transfer.

Data availability

The data that support the findings of this study are available within this Article and its Supplementary Information. Any other data are available from the corresponding authors on request.

Acknowledgements

The work was supported by the National Science Foundation under CBET 1912885 (F.L.). This research used resources of the Advanced Photon Source, US Department of Energy (DOE), Office of Science User Facility, operated for the DOE Office of Science by Argonne National Laboratory under contract no. DE-ACO2-06CH11357. The use of the Stanford Synchrotron Radiation Lightsource (SSRL), SLAC National Accelerator Laboratory, was supported by the US DOE, Office of Science, Office of Basic Energy Sciences, under contract no. DE-ACO2-76SF00515. This research used the electron microscopy resources of the Center for Functional Nanomaterials (CFN), US DOE, Office of Science User Facility, at Brookhaven National Laboratory under contract no. DE-SC0012704. Y.Z. and F.L. thank the beamline scientist R. Davis at SSRL for help with the hard XAS measurements.

Author contributions

F.L. conceived and led the project. F.L. and Y.Z. designed the experiments. Y.Z. performed the materials synthesis, electrochemical tests, synchrotron measurements and data analysis. A.H. and D.X. assisted with the XFM measurements. D.X. assisted with the hard XAS measurements. S.S. and D.N. performed the soft XAS measurements. S.H. performed the TEM measurements and data analysis. F.M.M. participated in the data discussion. R.B.M. participated in the experimental design and data discussion. L.L. assisted with the XFM measurements and participated in the discussion and data analysis. Y.Z. and F.L. wrote the manuscript with inputs from all the co-authors. All the authors approved the final draft of the manuscript.

Competing interests

The authors declare no competing interests.

Additional information

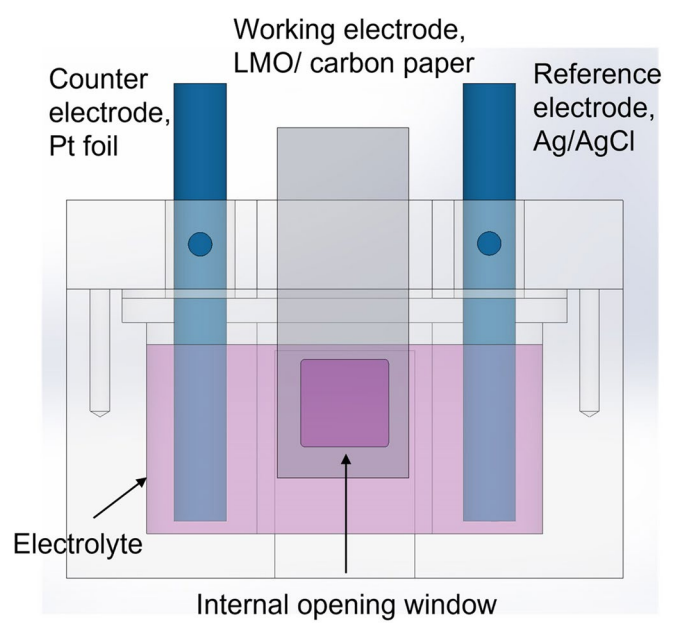
Extended data is available for this paper at https://doi.org/10.1038/s41565-023-01367-6.

Supplementary information The online version contains supplementary material available at https://doi.org/10.1038/s41565-023-01367-6.

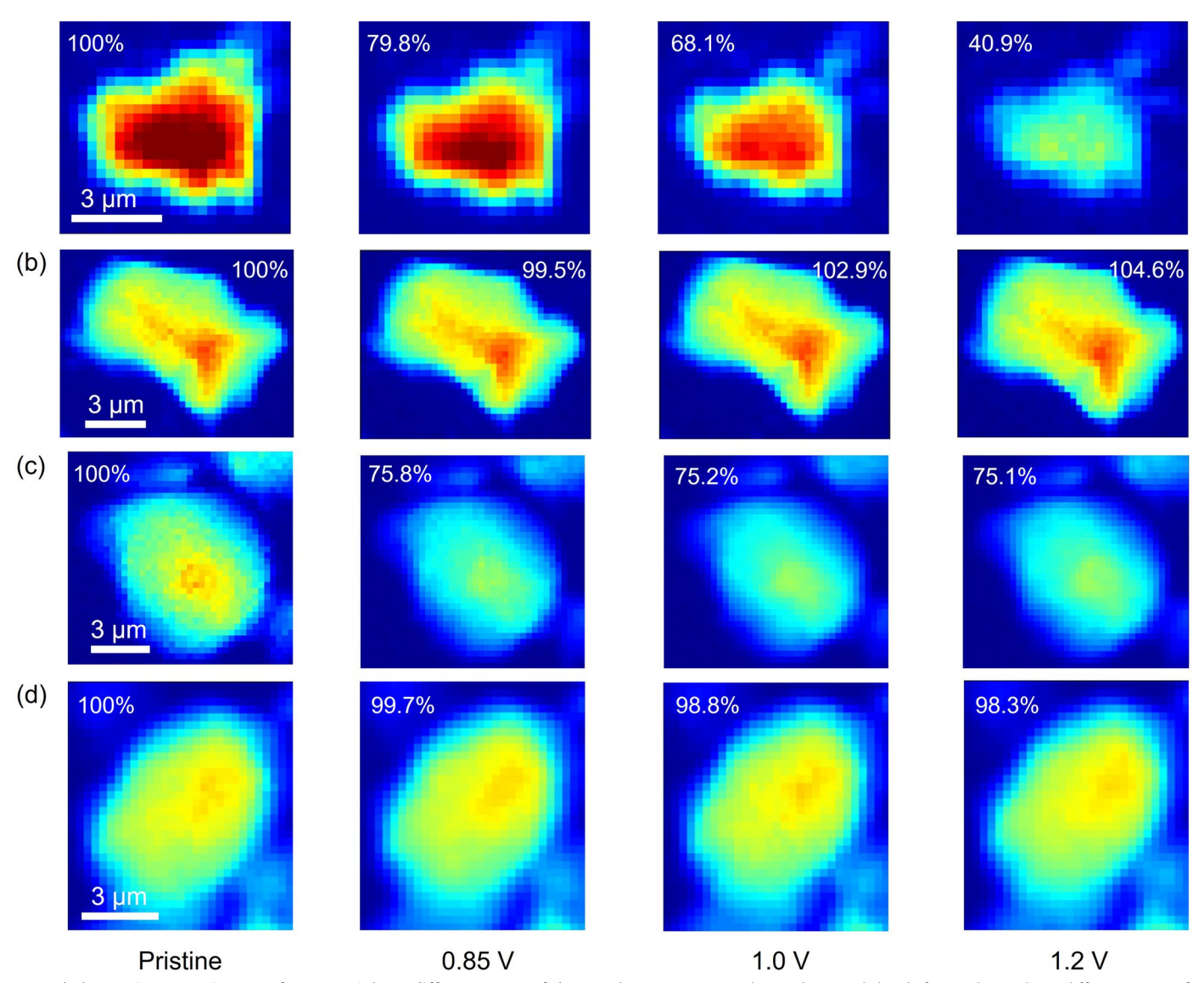
Correspondence and requests for materials should be addressed to Sooyeon Hwang, Luxi Li or Feng Lin.

Peer review information *Nature Nanotechnology* thanks Yong-Mook Kang and the other, anonymous, reviewer(s) for their contribution to the peer review of this work.

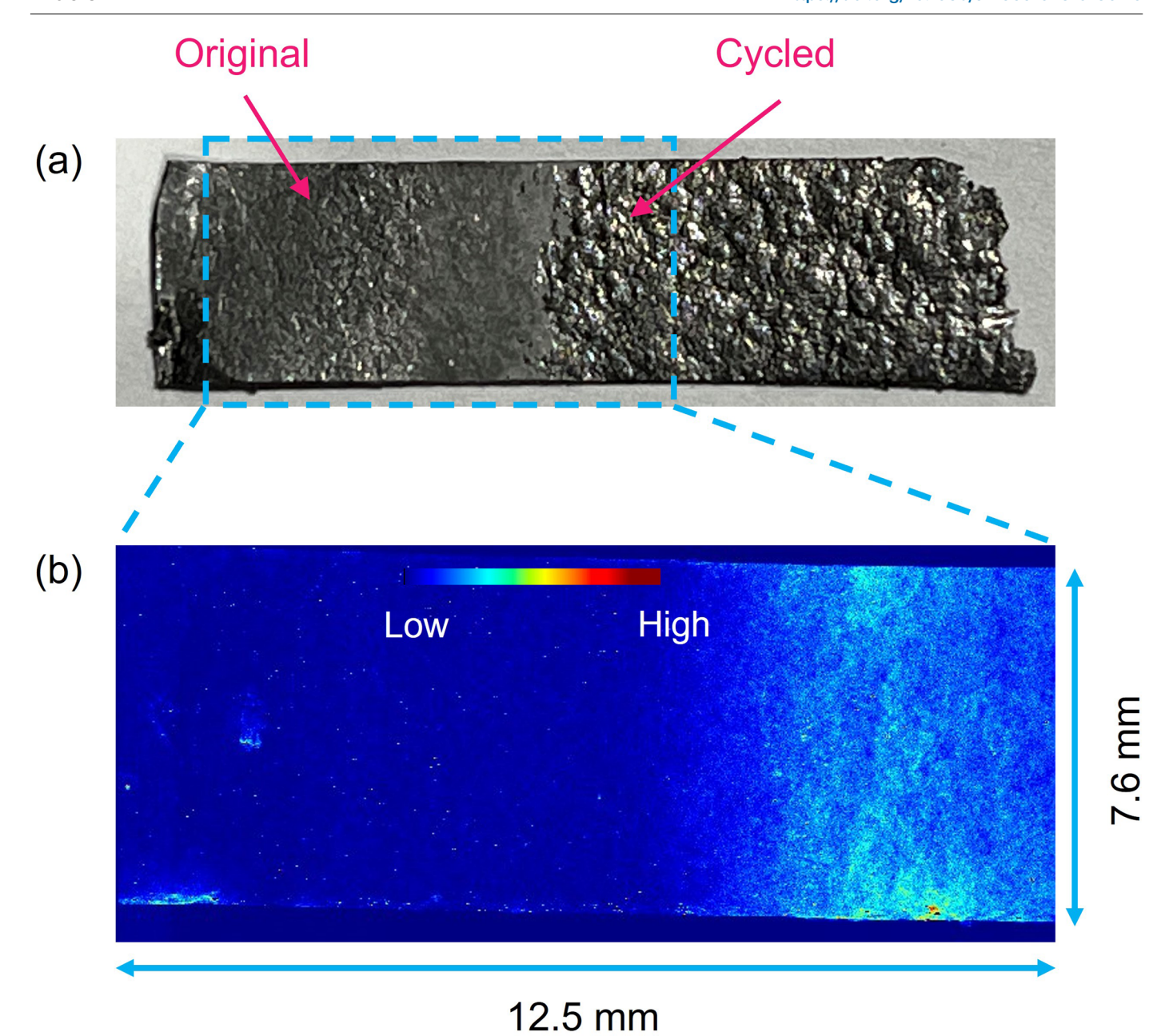
Reprints and permissions information is available at www.nature.com/reprints.



 $\textbf{Extended Data Fig. 1} | \textbf{Cell configuration for the in-situ X-ray fluorescence microscopy (XFM) experiment.} The three-electrode cell used for the in situ and operando X-ray fluorescence microscopy (XFM) experiment. The X-rays hit the electrode from the side of the current collector (carbon paper).}$

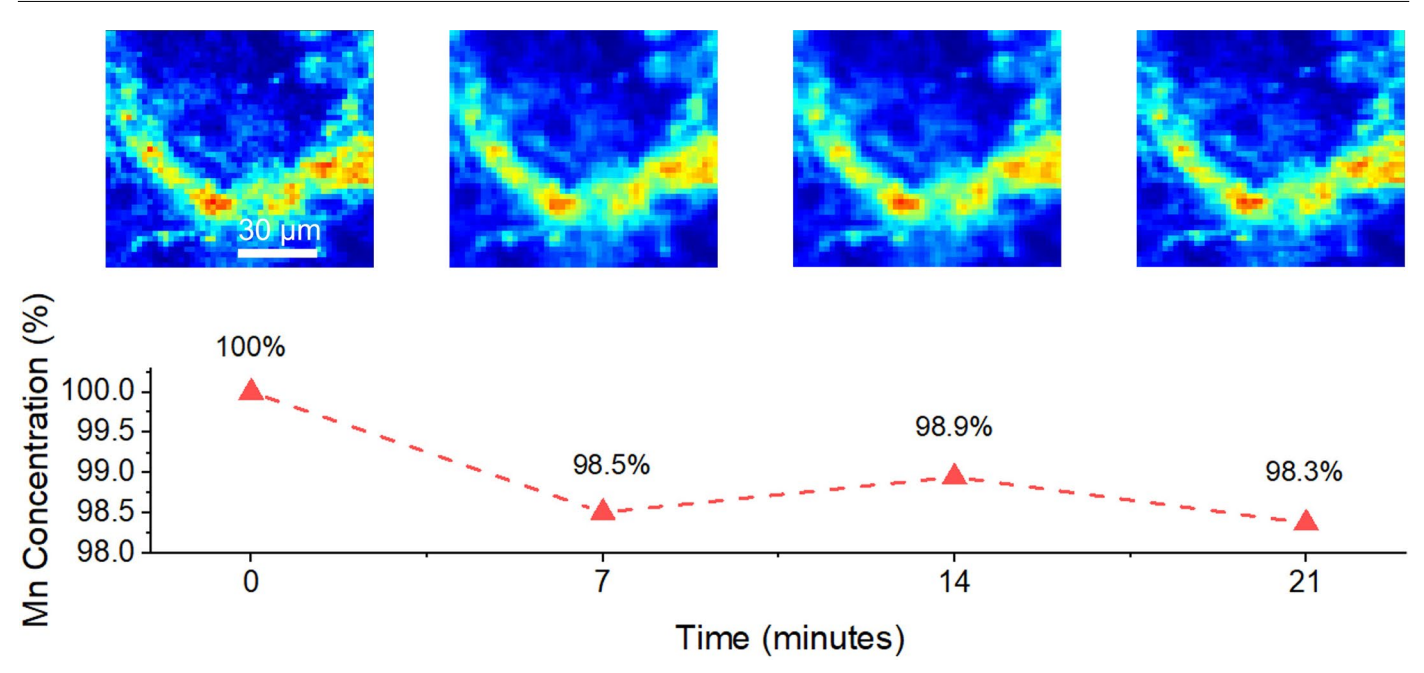


Extended Data Fig. 2 | XFM images of LMO particles at different states of charge. The XFM images at the single-particle level of LMO electrodes at different states of charge during the first cycle, showing a heterogeneous Mn D/R behaviours.

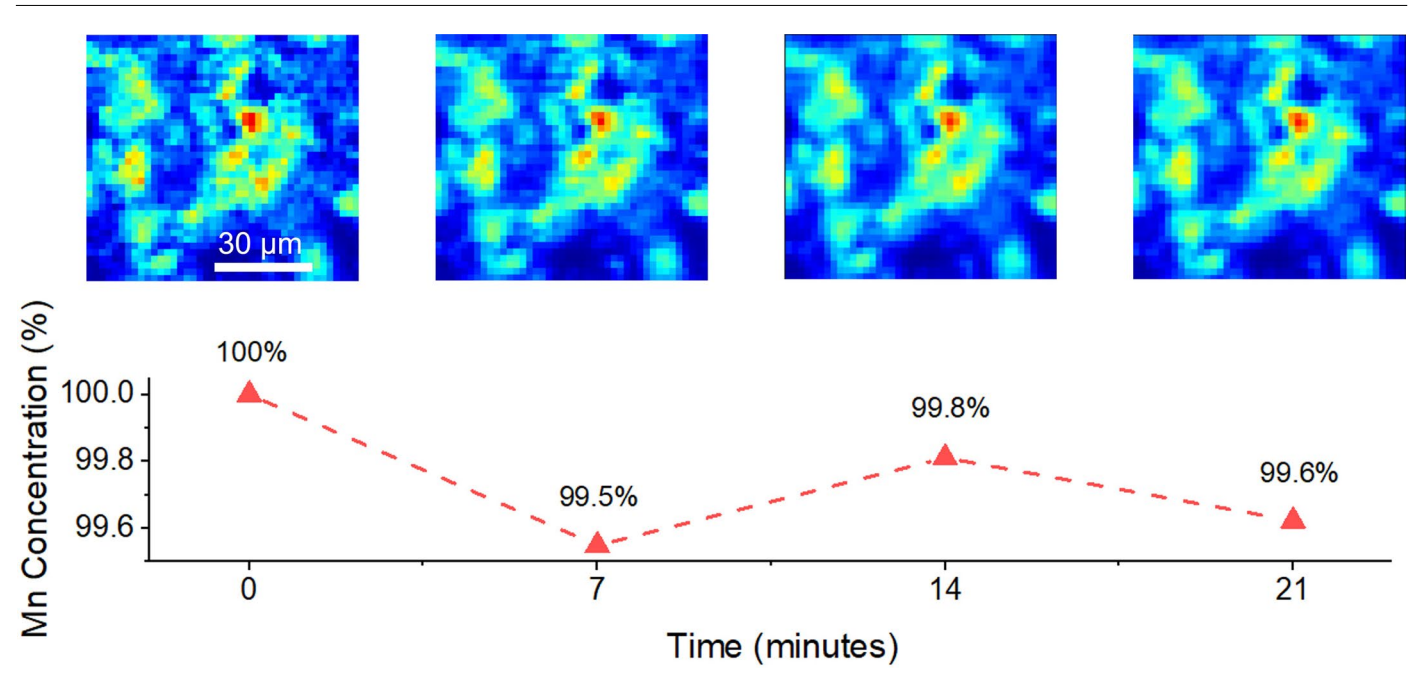


Extended Data Fig. 3 | **Mn deposition on the counter electrode.** (a) The photo of a graphite paper used as the counter electrode during electrochemical cycling, where the arrows indicate the original and cycled regions; (b) XFM image of the region labelled by blue frame in (a), showing a much higher Mn concentration in

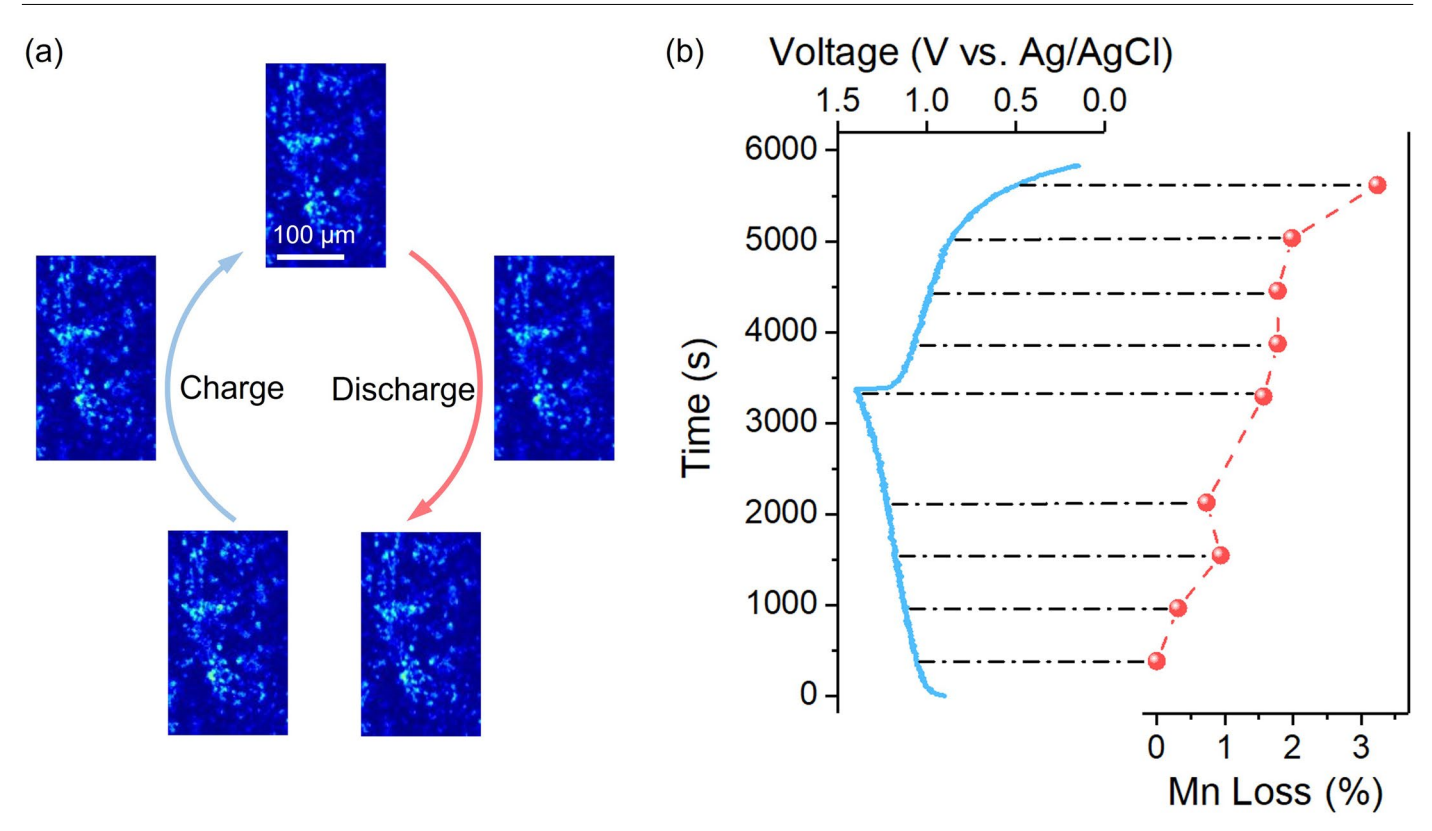
the cycled region and confirming that the dissolved Mn species can deposit on the counter electrode surface. Note that XFM is extremely elementally sensitive, the minor Mn concentration in the pristine graphite originates from the impurity.



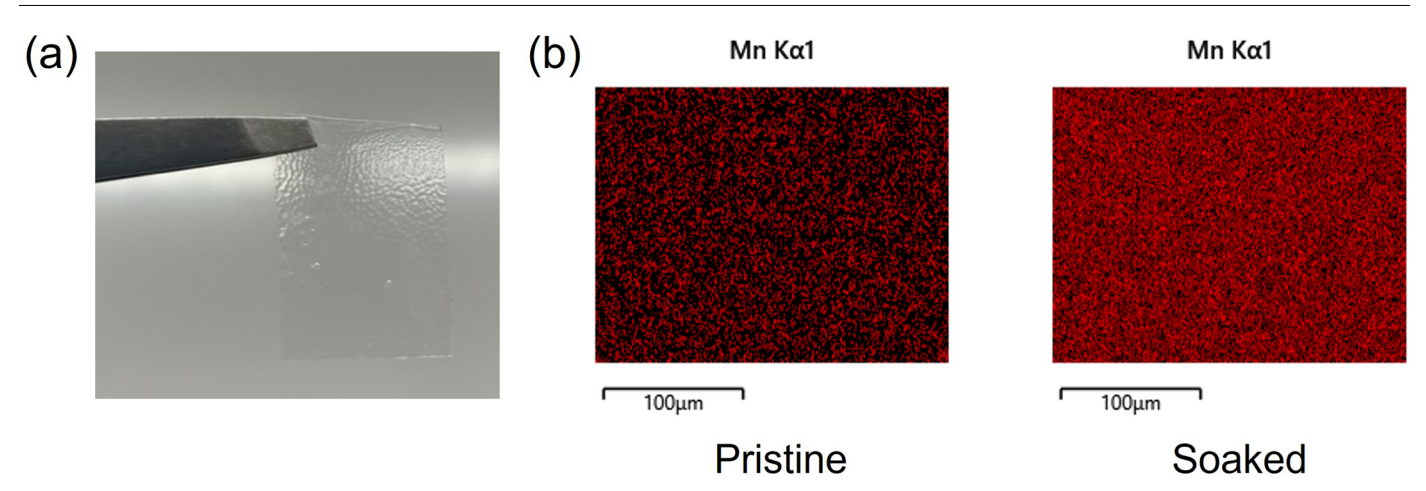
 $\textbf{Extended Data Fig. 4} | \textbf{Mn D/R dynamics of Mn}_3\textbf{O}_4 \textbf{held at 1.2 V.} The \, \textbf{Mn D/R dynamics of Mn}_3\textbf{O}_4 \textbf{held at 1.2 V.} The \, \textbf{CA protocol is applied for 21 minutes to keep the voltage at 1.2 V and monitor the \, \textbf{Mn concentration variation.} Each \, \textbf{XFM image takes 7 minutes.}$



 $\textbf{Extended Data Fig. 5} \ | \ \textbf{Mn D/R dynamics of MnO}_2 \ \textbf{held at 1.2 V.} \ \textbf{The Mn D/R dynamics of MnO}_2 \ \textbf{held at 1.2 V.} \ \textbf{The CA protocol is applied for 21 minutes to keep the voltage at 1.2 V and monitor the Mn concentration variation. Each XFM image takes 7 minutes.}$



Extended Data Fig. 6 | Mn D/R dynamics of LMO cycled in 2 M LiTFSI-TEGDME electrolyte. (a) The XFM images of Mn concentration in the LMO electrode during electrochemical cycling in 2 M LiTFSI in tetraethylene glycol dimethyl ether (TEG-DME) solvents; (b) the corresponding Mn D/R behaviours during the first cycle.



 $\textbf{Extended Data Fig. 7} | \textbf{Trapped Mn ions in the Nafion membrane. (a)} | \textbf{The photos of casted Nafion membrane; (b)} | \textbf{the EDS mapping of Mn element for pristine and soaked Nafion membranes.} \\ \textbf{The Mn signal in pristine membranes is caused by the uncertainty from the instrument, the actual Mn atomic ratio is zero.} \\ \textbf{The Mn signal in pristine membranes is caused by the uncertainty from the instrument, the actual Mn atomic ratio is zero.} \\ \textbf{The Mn signal in pristine membranes} | \textbf{The Mn signal in pristine membr$